Hybrid Photoelectrocatalytic TiO2-Co3O4/Co(OH)2 Materials Prepared from Bio-Based Surfactants for Water Splitting

Fanny Duquet, Valérie Flaud, Christina Villeneuve-Faure, Matthieu Rivallin, Florence Rouessac, Stéphanie Roualdès

Article

Hybrid photoelectrocatalytic TiO_2-Co_3O_4/$Co(OH)_2$ materials prepared from bio-based surfactants for water splitting

Fanny Duquet[1,*], Valérie Flaud[2], Christina Villeneuve-Faure[3], Matthieu Rivallin[1,*], Florence Rouessac[1] and Stéphanie Roualdès[1]

[1] Institut Européen des Membranes (IEM), UMR 5635, University of Montpellier, ENSCM, CNRS, 34095 Montpellier, France ; florence.rouessac@umontpellier.fr (F.R) ; stephanie.roualdes@umontpellier.fr (S.R)
[2] Institut Charles Gerhardt, ICGM, UMR 5253, University of Montpellier, ENSCM, CNRS, 34095, Montpellier Cedex 5, France ; valerie.flaud@umontpellier.fr (V.F)
[3] LAPLACE, Université de Toulouse, UPS, CNRS, INPT, 31062 Toulouse, France ; christina.villeneuve@laplace.univ-tlse.fr (C.V.-F)

* Correspondence: fanny.duquet@umontpellier (F.D) and matthieu.rivallin@umontpellier.fr (M.R)

Abstract: The development of new photoanode materials for hydrogen production and water treatment is in full progress. In this context, hybrid TiO_2-Co_3O_4/$Co(OH)_2$ photoanodes prepared by the sol-gel method using biosurfactants are currently being developed in our group. The combination of the TiO_2 with cobalt-based compound significantly enhances the visible absorption and electrochemical performance of the thin films, which is mainly due to an increase in the specific surface area and a decrease in the charge transfer resistance at the surface of the thin films. The formation of these composites allows a 30-fold increase in the current density when compared to cobalt-free materials, with the best TiO_2-CoN0.5 sample achieving a current of 1.570 $mA.cm^{-2}$ and a theoretical H_2 production rate of 0.3 $\mu mol.min^{-1}.cm^{-2}$ under xenon illumination.

Keywords: composite materials, photoanodes, water splitting, heterojunctions, titanium oxides, cobalt oxides

1. Introduction

One of the most attractive solutions for reducing air pollution and slowing down global warming is the use of "green" hydrogen as an energy carrier. By using a photoelectrochemical cell (PEC) at the interface between water electrolysis and photocatalysis, hydrogen can be produced without greenhouse gas emissions [1–3]. Moreover, the use of partially polluted water as a resource for this cell would allow the coupling of green hydrogen production with tertiary water treatment [4–8]. In this respect, work on the components of this cell, especially the photoanodes, is essential to make such a system competitive.

The photoanode plays a key role in a PEC. It receives the light and generates the charges necessary for the oxidation reaction of the water on its surface and, consequently, for the production of hydrogen at the counter electrode, as well as for the mineralization of the organic pollutants present in the water (in the case of polluted water as a resource). This must be of the semiconductor type, and our choice fell on TiO_2, already known for its photocatalytic properties, among other advantages [9–11]. However, TiO_2 has disadvantages such as low absorption in the solar spectrum (limited to the UV range), rapid charge recombination and low electronic conductivity [12–14]. The formation of a heterojunction combining the n-type TiO_2 semiconductor with a p-type semiconductor

can improve these properties [15–18]. Cobalt oxide has already proven itself as a dopant for TiO_2 due to its high catalytic activity, low cost, stability in neutral and alkaline environments and ability to be used as a bifunctional electrode [19,20]. Co_3O_4 has interesting electronic properties which are an advantage for our application, and also a direct band gap between 1.5 and 2.5 eV, which is essential for improving absorption in the visible range [21–25]. Thus, this p-type semiconductor was chosen in this study to realize an n-TiO_2 | p-Co_3O_4 type heterojunction.

This kind of heterojunction has demonstrated enhanced electrochemical performance through diverse synthesis routes such as hydrothermal route [26,27], anodization [28], atomic layer deposition [29], metal organic chemical vapor deposition [30], impregnation [31]. Regarding the sol-gel synthesis, it is rarely the only route used for n | p materials, but it is often coupled with other synthesis routes. In this study, our goal was to create photo-anodic materials using titanium and cobalt oxides along with different bio-sourced surfactants via a new one-step sol-gel method. This synthesis method is cost-effective, easy to implement, and could be transferred to other different types of heterojunctions, allowing for a broader study. We have decided to use three different surfactants and to introduce cobalt oxide in two molar ratios (HNO_3/TTIP/$Co(NO_3)_2 \bullet 6\ H_2O$ = 1/1/0.25 and 1/1/0.5) to allow a high degree of modularity in terms of chemical composition, structural properties and, therefore, functional properties of the photoanodes in order to optimize their performances in water splitting.

2. Results and Discussion

2.1. Structural and textural characterization

TiO_2/Co_3O_4 samples prepared with the GB surfactant were selected to illustrate the XRD powder results in **Figure 1** with the diffractograms of TiO_2-GB, TiO_2-CoN0.25-GB, TiO_2-CoN0.5-GB and CO_3O_4-GB. In order to compare the crystal structures of the TiO_2-Co_3O_4 hybrid powders with those of the individual oxides, a Co_3O_4 powder (1:1:1 ratio) was synthesized using the same procedure as described above. On the TiO_2-GB diffractogram, the presence of TiO_2 characteristic peaks was noted at 25.4° for the anatase phase (A) and at 27.5° for the rutile phase (R) [32]. For the Co_3O_4-GB powder, a characteristic peak of the spinel phase (S) was observed at 31.3° [33].

For XRD analysis, we used a copper (Cu) anticathode. The presence of cobalt (Co) in our samples, an element close to Cu in the periodic table, leads to a fluorescence phenomenon due to an absorption threshold close in energy to that of the incident beam. The resulting diagram exhibits a high continuous background with high noise, which obstructs proper observation of the Co_3O_4 peaks in the composite materials diffractograms (TiO_2-CoN0.25-GB and TiO_2-CoN0.5-GB). However, the three phases of the hybrid powder are observable, and it is seen that the addition of Co_3O_4 does not affect the position of the diffracted TiO_2 peaks, but does appear to affect the anatase/rutile phase ratio.

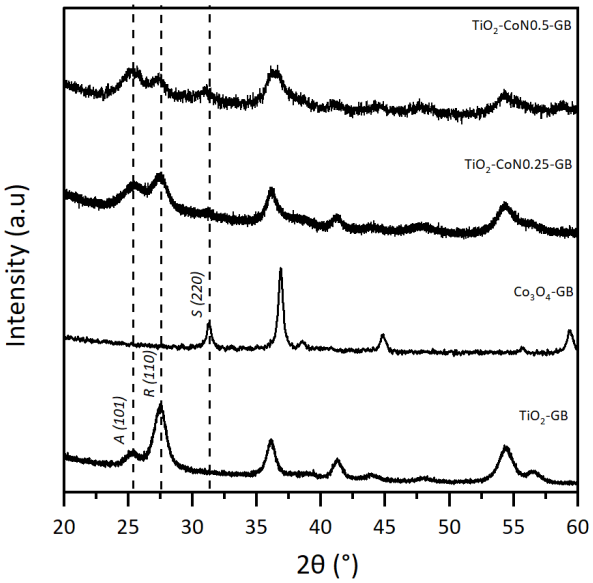

Figure 1. Powder diffraction patterns for TiO_2-GB, CO_3O_4-GB, TiO_2-CoN0.25-GB, and TiO_2-CoN0.5-GB.

To know more, the anatase and rutile proportions were calculated by Rietveld refinement and are reported in Table S1 [34]. As already displayed in our previous work, the rutile phase predominates in the TiO_2 powders, but the anatase/rutile ratio varies depending on the surfactant used [35]. For the hybrid powders, the influence of the addition of cobalt oxide on the TiO_2 phases is illustrated in the histogram (**Figure 2**). It can be seen that the presence of the spinel phase causes a decrease in the proportion of the rutile phase in favor of the anatase phase to the point where it becomes dominant. It appears that the presence of Co_3O_4 inhibits the effect of the surfactant on the formation and stability of the anatase phase [36–38].

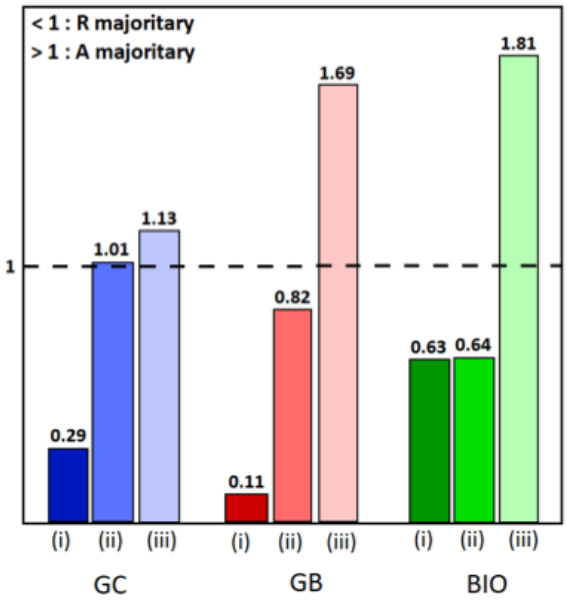

Figure 2. Histograms of anatase/rutile ratios (i) for TiO_2 type samples, (ii) for TiO_2-CoN0.25 type samples and, (iii) for TiO_2-CoN0.5 type samples.

Calculation of the crystallite size was determined using Scherrer formula (1) with K as the form factor (0.9 value for a spherical crystallite shape), λ as the CuKα wavelength

(in nanometers), HW as the half-width value (in radians), and θ as the corresponding diffraction angle (in radians). The results suggest cobalt oxide has a direct impact on the formation and size of anatase and rutile crystallites (refer to Table S2).

The crystallite size of the hybrid powders decreases independently of the type of surfactant, reaching values centered on 4 nm for the anatase phase and 6 nm for the rutile phase. The amount of cobalt oxide does not seem to have any influence, since the two ratios 0.25 and 0.5 induce similar crystallite size values. It can be concluded that the formation of the hybrid material containing the TiO_2/Co_3O_4 phase mixture allows a smoothing of the crystallite size of the different TiO_2 phases.

$$d = \frac{K \times \lambda}{HW \times \cos\theta} = \frac{0{,}9 \times 0{,}15406}{HW \times \cos\theta} \quad (1)$$

The BET isotherms for the hybrid materials show the same pattern, indicating the dual presence of microporosity and mesoporosity, as observed for TiO_2-GC in the previous work (Figure S1). Table 1 shows the specific surface areas, average sizes and pore distributions of the materials. The specific surface area of the materials formed by the two oxides is higher than that of the TiO_2 powders and increases with the amount of cobalt oxide. In fact, we find the following hierarchy TiO_2-CoN0.5 > TiO_2-CoN0.25 > TiO_2 in terms of specific surface area. This increase is particularly remarkable for GB and BIO samples, which reach specific surface areas of 97 and 126 $m^2.g^{-1}$ respectively for the highest Ti/Co ratio (0.5). For GC, whose specific surface area without cobalt was by far the highest, the increase is less, but the threshold of 126 $m^2.g^{-1}$ is reached for the same ratio (0.5). However, the average pore size of the hybrid materials does not change much between the different samples, making it difficult to correlate with the specific surface area. It seems that, as with the crystallite size above, the pore size for all TiO_2-Co_3O_4 materials homogenizes with the addition of cobalt to an average value of about 4.7 nm. The difference in specific surface area despite almost identical pore size could be explained by a difference in the size of the "mixed" aggregates.

Table 1. BET results.

Samples	BET surface area (m^2/g)	Adsorption Average Pore Width BET (nm)	Pore size distribution (nm)
TiO_2-GC	101	2.66	Bimodal: 4 nm - 11 nm
TiO_2-CoN**0.25**-GC	112	4.85	Bimodal: 3.5 nm - 5 nm
TiO_2-CoN**0.5**-GC	126	4.27	Unimodal: 3.5 nm
TiO_2-GB	31	4.95	Bimodal: 4 nm - 60 nm
TiO_2-CoN**0.25**-GB	91	4.56	Bimodal: 3.5 nm - 5 nm
TiO_2-CoN**0.5**-GB	97	4.86	Unimodal: 3.5 nm
TiO_2-BIO	16	8.77	Bimodal: 3 nm - 9 nm
TiO_2-CoN**0.25**-BIO	88	5.82	Bimodal: 3.5 nm - 5 nm
TiO_2-CoN**0.5**-BIO	126	4.07	Unimodal: 3 nm

The pore size distribution for the TiO_2-CoN0.25 materials is similar, with all three samples showing a bimodal distribution centered at around 3.5 nm and 5 nm. A monodispersity is observed for the 3.5 nm pore size and a polydispersity for the 5 nm pore size (**Figure S2**). The same observation can be made for the TiO_2-CoN0.5 type materials, which have the highest cobalt loading, with the three samples showing the same type of distribution. For the 0.5 ratio, it can be observed a unimodal and monodispersed distribution centered at around 3.5 nm for GC and GB and closer to 3 nm for BIO (**Figure S3**). Through the pore size distribution, we again find a homogenization effect of the properties of the samples due to the addition of cobalt oxide. Based on the above results, only the samples synthesized with the GC surfactant with the highest specific surface

area (TiO_2-GC, TiO_2-CoN0.25-GC and TiO_2-CoN0.5-GC) will be further characterized in the following.

2.2. Morphological and chemical characterization

SEM images of the surface of the three GC-based thin films deposited on ITO support are shown in **Figure 3**. The surface of the TiO_2-GC thin film (**Figure 3.a**) is smooth and free of imperfections, which is not the case with the addition of Co_3O_4. At a ratio of 0.25 (**Figure 3.b**), cracks appear, probably due to the change in surface tension caused by the addition of Co, but the surface of the thin film remains smooth.

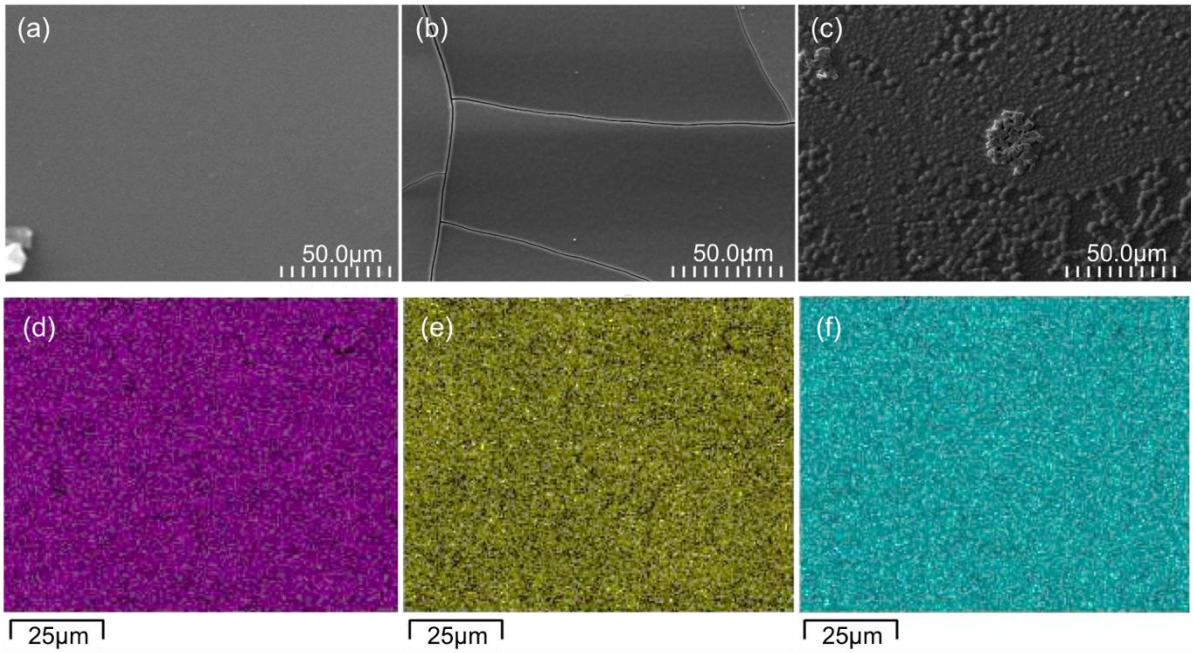

Figure 3. SEM images of the surface (a) TiO_2-GC, (b) TiO_2-CoN0.25-GC (c) TiO_2-CoN0.5-GC and EDX mapping of TiO_2-CoN0,5-GC sample, in pink (d) distribution of Ti element, in yellow (e) Co element, in blue (f) O element.

On the other hand, when the ratio is increased to 0.5 (**Figure 3.c**), the appearance of the thin film surface is completely changed. A surface consisting of aggregates of TiO_2 and Co_3O_4 nanoparticles is observed. This was confirmed by a 5 µm × 5 µm surface topography measurement by AFM (not shown) which demonstrated an increase in the arithmetic surface roughness from 0.8 nm for TiO_2 to 3.8 nm and 11.5 nm for Co_3O_4 ratios of 0.25 and 0.5, respectively. The thicknesses of the thin films are approximately the same with a total value of 1100 ± 350 nm.

The EDX analysis indicates that the Ti, Co, and O elements are uniformly distributed throughout the TiO_2-CoN0.5-GC thin film (**Figure 3.d, e**, and **f**). This observation is also true for the other TiO_2-CoN0.25-GC thin film, whose EDX profiles are not shown here. Via a semi-quantitative study of EDX maps, the elemental composition ratios Co/Ti for the TiO_2-CoN0.25-GC and TiO_2-CoN0.5-GC samples are determined to be 0.27 and 0.59, respectively.

XPS analysis was performed to determine the surface composition of the thin films. For the hybrid materials, the total spectrum of the TiO_2-CoN0.5-GC sample is shown in **Figure 4.a** and is similar to those of the other samples regardless of the ratio used. In the total spectrum, we observe the presence of the same chemical elements as in the TiO_2 thin

films (C, O, Ti and Sn, In from the ITO substrate) and, in addition, the cobalt Co 2p appears at high binding energies [35]. The Co Auger peak corresponds to the emission of an electron during the de-excitation of the Co atom.

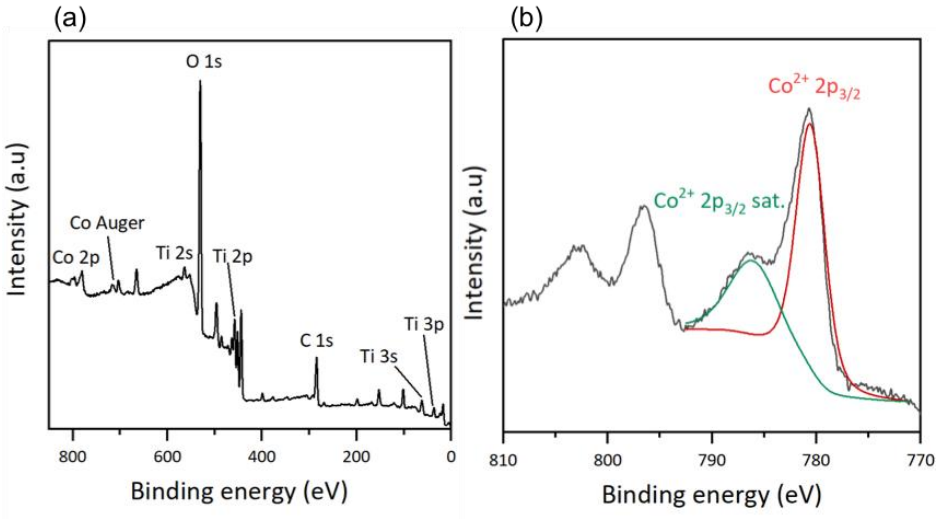

Figure 4. XPS results (a) survey of TiO_2-CoN0.5-GC, (b) Co2p scan after deconvolution of TiO_2-CoN0.5-GC.

To verify the nature of the cobalt on the surface of the thin films, a high-resolution deconvolution of the Co 2p spectrum was performed (**Figure 4.b**). A main peak related to Co^{2+} $2p_{3/2}$ at 780.5 eV and its satellite peak at 786.0 eV can be identified. The presence of a satellite peak is characteristic of the Co^{2+}, outgoing electron interacting with a valence electron and exciting it, thereby shaking it to a higher energy level. As a consequence, the energy of the core electron is reduced and a satellite structure appears a few eV below the core level position, it's a shake-up type peak satellite [39,40]. Cobalt oxide Co_3O_4 is a mixed valence compound, cobalt exists in two oxidation states: Co^{2+} and Co^{3+}. However, the deconvolution shows only the presence of Co^{2+}, suggesting that cobalt in its oxidation state (III) does not exist on the surface of mixed thin films. According to Biesinger, M. C. et al, the position and shape of the Co^{2+} $2p_{3/2}$ peak indicates the presence of cobalt in the form of $Co(OH)_2$[41]. Since XPS gives access to a surface measurement, the cobalt oxide has probably adsorbed water molecules, inducing the formation of Co-O bonds, the oxygen coming from the water molecules. This hydroxide form on the surface of the materials applies to both mixed materials regardless of the Co ratio.

To evaluate the effect of the addition of cobalt oxide on the titanium oxide, the Ti 2p spectra for the three samples synthesized from the GC surfactant are shown in **Figure 5**.

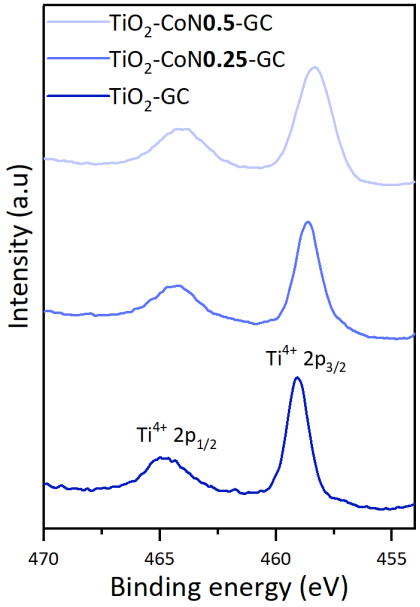

Figure 5. Comparison of Ti 2p scan of the three thin films.

The Ti 2p spectra display two symmetrical peaks corresponding to Ti $2p_{1/2}$ and Ti $2p_{3/2}$, representing Ti^{4+} in TiO_2. With the incorporation of Co, there is a subsequent shift to lower binding energies (+0.5 eV for TiO_2-CoN0.25 and 0.2 eV for TiO_2-CoN0.5), indicating the occurrence of electron transfer between Co_3O_4/$Co(OH)_2$ and TiO_2. This transfer establishes an interaction between them, which can facilitate surface charge separation and enhance the photocatalytic activity of the thin films [42,43].

2.3. Optical Properties

In order to determine the evolution of the absorption of the thin films in the visible region, UV-visible-NIR spectra were studied. TiO_2 is an oxide that absorbs mainly in the UV region (from 100 to 400 nm), while Co_3O_4 absorbs in the visible region (from 400 to 780 nm). **Figure 6** shows the absorption spectra of the samples. The TiO_2 thin film spectrum is characteristic of TiO_2 with absorption at wavelengths below 400 nm. With the addition of a small amount of cobalt oxide, a shift of the absorption towards the visible region is observed as well as an increase in absorbance compared to the cobalt-free sample.

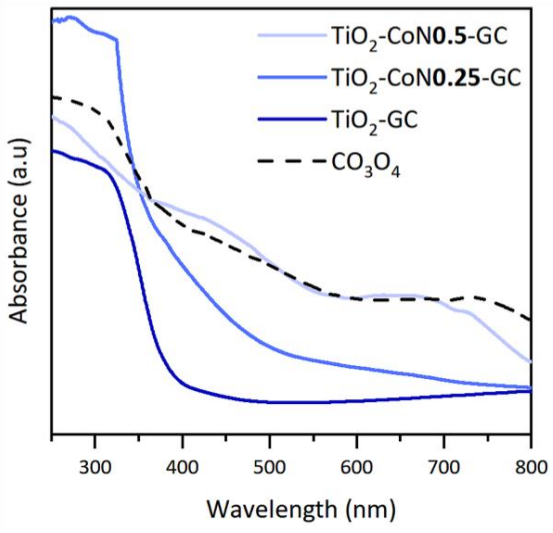

Figure 6. UV-visible spectroscopy data with an absorption spectra of GC samples and Co_3O_4.

The absorption spectrum of the TiO_2-CoN0.5 thin film shows that increasing the Co content reinforces the above observations. Therefore, it can be concluded from the absorption spectra that the addition of cobalt oxide has the desired effect of increasing the absorption in the visible region for the TiO_2-CoN0.25 and TiO_2-CoN0.5 samples. Figure 6 shows that the absorption profile of the cobalt oxide is similar to that previously highlighted for the TiO_2-CoN0.5 thin films, indicating that the cobalt oxide is at the origin of the improvement in the optical properties of the mixed materials. To determine the band gap of the thin films, the Tauc diagram was constructed by plotting the coefficient $(\alpha h\nu)^n$ as a function of energy E in eV. The value of the band gap was obtained by extrapolating the linear portion of the curve at the intersection of this line with the x-axis.

The absorption coefficient α (cm^{-1}) and the frequency ν (Hz) can be determined from equations (2) and (3), where A is the absorbance, e is the thickness of the thin film (cm), c is the speed of light ($m.s^{-1}$), and λ is the wavelength (m).

$$\alpha = \frac{A}{100} \times \frac{1}{e} \quad (2)$$

$$\nu = \frac{c}{\lambda} \quad (3)$$

The coefficient n is related to the type of band gap, namely n = 0.5 for an indirect band gap (anatase phase) or n=2 for a direct band gap (rutile and spinel phases).

The energy E (eV), can be determined using equation (4), where q is the elementary charge ($1.6.10^{-19}$ C) et and h is Planck's constant ($6.63.10^{-34}$ J.s):

$$E = \frac{h\nu}{\mathrm{q}} = \frac{hc}{\lambda \mathrm{q}} \quad (4)$$

The theoretical value of the indirect band gap of the anatase phase is 3.2 eV and that of the direct band gap of the rutile phase is 3.0 eV. For the spinel phase of cobalt oxide, the direct band gap is between 1.5 and 2.5 eV. It is interesting to compare these theoretical values with the experimental values determined by the Tauc plot and presented in Table 2, distinguishing between the indirect and direct band gaps. For the TiO_2 thin film, an indirect band gap lowers that of the anatase phase is obtained, with a value of 2.87 eV. This difference between the experimental and theoretical values is not surprising, considering the minority of the anatase crystal phase in the compound (22%). For the direct band gaps, the experimental value is 3.37 eV, which is higher than the theoretical value for the rutile phase. For the TiO_2-CoN0.25 thin film, the indirect band gap shows values close to those of the indirect band gap of the TiO_2 film with a slight decrease. For the direct band gap, two energy levels can be displayed. The first energy level (2.73 eV) is close to the value of the cobalt oxide band gap, while the second energy level (3.54 eV) is close to the theoretical value for the rutile phase. Therefore, the band gaps of the three crystalline phases present in TiO_2-CoN0.25-GC can be effectively observed. Finally, the TiO_2-CoN0.5-GC film has a band gap value of 3.11 eV, which is close to that of the rutile phase, which is not the dominant phase in this material (A: 37% - R: 33% - S: 30%).

It is therefore difficult to attribute this value to either phase, rutile or spinel. However, given the previous values found for the rutile phase (3.37 eV and 3.54 eV) and for the spinel phase (2.73 eV), we can imagine that the value of 3.11 eV is an intermediate value that is effectively representative of the band gap of this material. In this type of thin

film (with a high cobalt content), no reliable values for the indirect band gap of the anatase phase could be obtained. Finally, calculations of band gap values from Tauc diagrams confirm the presence of the different crystalline phases and the effect of cobalt oxide: the addition of cobalt oxide to the materials would lower the band gap energy and thus shift the absorption of the materials into the visible region.

2.4. Electronic Properties

In order to compare the electronic conductivity of thin films at the nanometer scale, current measurements were made at negative voltages using C-AFM. For an n-type semiconductor such as TiO_2, the current flows best at negative voltages, and conversely for a p-type semiconductor such as Co_3O_4, the current flows best at positive voltages. However, the position of the energy levels of the band structure of the semiconductor in relation to the Fermi level of the metal forming the tip (here PtSi) also has an effect on the current collected. The choice of negative or positive voltage does not necessarily define the nature of the majority carriers, n or p. In our case, it is more relevant to present the results for a negative voltage, since the films mostly contain TiO_2.

In the topography maps in **Figure 7.a,b,c** the presence of cobalt oxide seems to induce a smoothing of the thin films with a decrease in crystallite aggregation.

Figure 7.d,e,f represents the corresponding current, the distribution is heterogeneous for all the samples, as can be seen from the current maps with two different colors. The percentage of conductive area for the hybrid thin films increases from 20% for TiO_2-GC to 85% and 98% for TiO_2-CoN0.25-GC and TiO_2-CoN0.5-GC, respectively (**Table S3**).

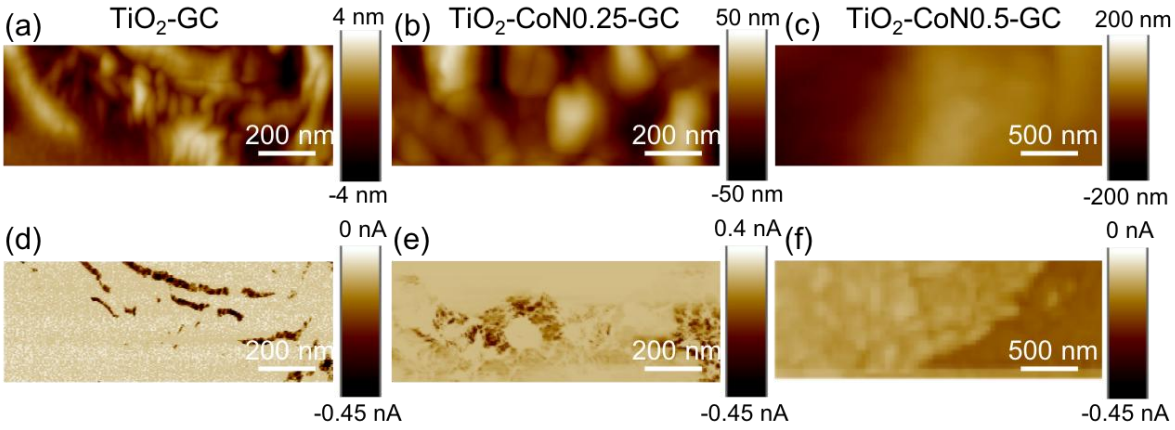

Figure 7. (a, b and c) Topography and (d, e and f) current maps for the corresponding areas below for TiO_2-GC samples at -5 V, TiO_2-CoN0.25-GC at -9 V and TiO_2-CoN0.5-GC at -9 V respectively.

In contrast to the percentage of conductive area, the collected current in the conductive area (i.e. dark area) decreases with the Co ratio ranging from -0.45 nA for TiO_2-GC to -0.035 nA for TiO_2-CoN,0.25 and to -0.045 nA/-0.122 nA for TiO_2-CoN0.5-GC. As it can be seen, for the thin film with the highest cobalt ratio, two current values are collected, proving the inhomogeneous current distribution in the bulk. This could be evidence of the presence of a large aggregate of TiO_2 and Co_3O_4 nanoparticles, with the most conductive areas associated with cobalt oxide, which is known to have better electrical conductivity than titanium oxide. Since the conductive surface and the current collected in the conductive surface exhibit different behavior with Co ratio, it is important to compare the average current over similar surfaces. This mean current ranges from -71 pA for TiO_2 to -28 pA and -47 pA for 0.25 and 0.5 Co ratio respectively. Thus, the presence of cobalt oxide does not have the expected effect on the electronic conductivities

from a nanometric point of view. In fact, Co_3O_4 has a higher intrinsic conductivity than TiO_2. However, this effect was limited by other parameters such as (i) the reduction of the crystallite sizes, (ii) the modification of the ratio between anatase and rutile phases or the modification of the band gap.

With the aim of studying the electronic conductivity at thin film/electrolyte interface, the electrical model corresponding to our system consists of one resistor Rs connected in series with two resistor-CPE pairs (Rp-1/CPE-p-1 and Rp-2/CPE-p-2) connected in parallel [44].

The resistor Rs is characteristic of the electrolyte and the two pairs Rp-1/CPE-p-1 and Rp-2/CPE-p-2 correspond to the ITO support and the supported thin film, respectively. These components are shown in **Figure 8.a**, using a Nyquist plot as example.

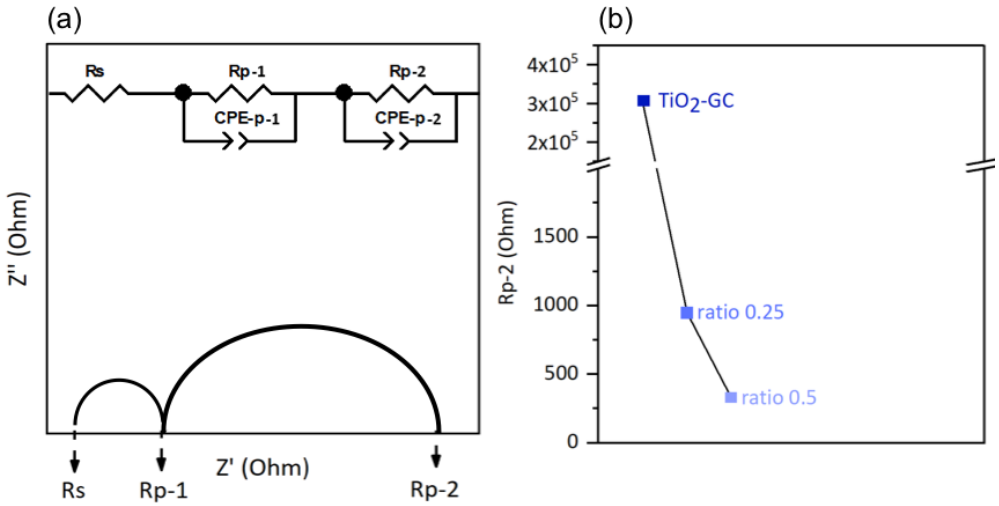

Figure 8. (a) Example of a Nyquist plot and illustration of the equivalent circuit model used in this study; Z' = ReZ and Z'' = -ImZ and (b) charge transfer resistance Rp-2.

The charge transfer resistances of the electrolyte (Rs) and at the ITO-substrate interface (Rp-1) are not expected to vary from sample to sample because the electrolyte and ITO substrate are the same for all samples.

However, the ITO/thin film interface may slightly affect the Rp-1 value depending on the nature of the thin film in question. The values of Rs and Rp-1 obtained from the Nyquist plots in the dark are listed in **Table S4**. Differences in these values depending on the nature of the studied thin film are observed without being able to explain them. However, we mainly discuss here the charge transfer resistance at the thin film/electrolyte interface (Rp-2) and its evolution according to the nature of the thin films. The lower the Rp-2 resistance, the easier the electron transfer at the material/electrolyte interface, which generally leads to a better electron transfer in the whole electrochemical cell, for a higher faradic efficiency. The onset potential used for the EIS is the minimum potential required to initiate the electrolysis reaction of water. The values of the onset potentials chosen in this study are derived from the cyclic voltammetry curves presented in the following section and are listed in **Table S4**. The Nyquist plot of the different samples is shown in **Figure S4**, the decrease of the circular arc with the addition of cobalt oxide is obvious. The Rp-2 resistance value is shown in **Figure 8.b** for better visualization. For the TiO_2-GC, the Rp-2 value is 306 771 Ω, which is much higher than that of TiO_2-CoN0.25 (954 Ω) and TiO_2-CoN0.5 (332 Ω). The decrease in Rp-2 is less obvious when the amount of cobalt oxide is increased, but is still visible.

It can be concluded that the presence of cobalt oxide and the increase in specific surface is a great asset to reduce the charge transfer resistance of the hybrid thin films.

2.5. Photoelectrochemical Properties

To study the photoelectrocatalytic performance of thin films, we focused on three characteristics: the onset potential (E_{onset}), the maximum current intensity (I_{max}) and the photocatalytic activity of the materials. **Figure 9** illustrates the voltammograms collected under xenon irradiation for the three thin films.

The onset potential is defined as the voltage at which the water oxidation reaction initiates, theoretically equivalent to 1.23 V. In practice, this potential can range from 1.8 V to 2.7 V due to cathodic and anodic overvoltages and ohmic losses. The reaction requires less energy as the potential decreases. In this case, the introduction of CO_3O_4 decreases the potential significantly, lowering it from 1.84 V in the TiO_2 thin film to 1.62 V in both the TiO_2-CoN0.25 and TiO_2-CoN0.5 composite films.

For the maximum current intensities collected at 2 V, we can see a considerable improvement with the presence of cobalt: as the cobalt ratio increases, the current rises from 0.041 mA.cm^{-2} for TiO_2 to 0.529 mA.cm^{-2} for the 0.25 ratio, then to 1.570 mA.cm^{-2} for the 0.5 ratio.

To determine the photocatalytic activity of the thin films, we measured the difference in current intensity between the dark and xenon irradiation. The TiO_2 layer displayed a difference of 0.012 mA.cm^{-2}, while TiO_2-CoN0.25 and TiO_2-CoN0.5 exhibited differences of 0.025 and 0.004, respectively. Based on the relative magnitudes of the current intensities, only TiO_2 demonstrated significant photocatalytic activity. The presence of CO_3O_4 appears to interfere with the photocatalytic capabilities of TiO_2.

In conclusion, the addition of cobalt and creation of composite thin films have greatly improved the thermodynamic (E_{onset}) and kinetic (I_{max}) aspects of the water oxidation reaction. This enhancement comes at the detriment of TiO_2 photoactivity.

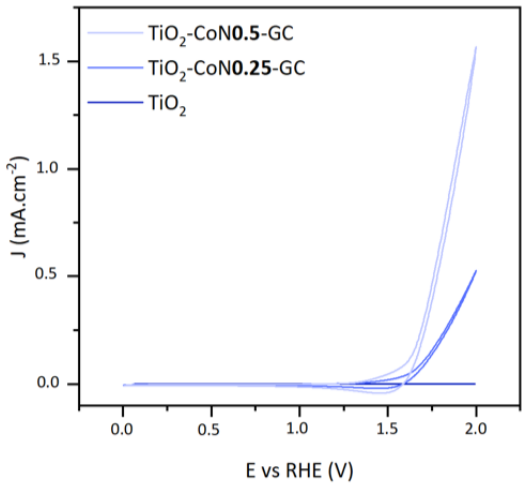

Figure 9. Cyclicvoltammetry curves of the three thin film under xenon irradiation.

The stability of the thin films was examined using photocurrent measurements. The stability of the top-performing TiO_2-CoN0.5 sample is shown in **Figure 10**. The chosen potential is the onset potential + 0.2V to ensure that non-negligible currents are obtained. At this potential, the thin film current density is stable at about 0.85 mA.cm^{-2} under xenon irradiation for 3 hours. From this curve, the theoretical amount of hydrogen produced n can be determined by utilizing Faraday's law (5).

In this equation, the electric charge Q is the electric intensity $i(t)$ integrated as a function of time t, n_{e-} represents the number of electrons involved in the H_2 reduction reaction, and F refers to Faraday's constant. A theoretical yield of 0.3 µmol.min^{-1}.cm^{-2} was calculated for the TiO_2-CoN0.5.

$$n = \frac{\int_0^t i(t)\,dt}{n_{e-} \times F} = \frac{Q}{n_{e-} \times F} \quad (5)$$

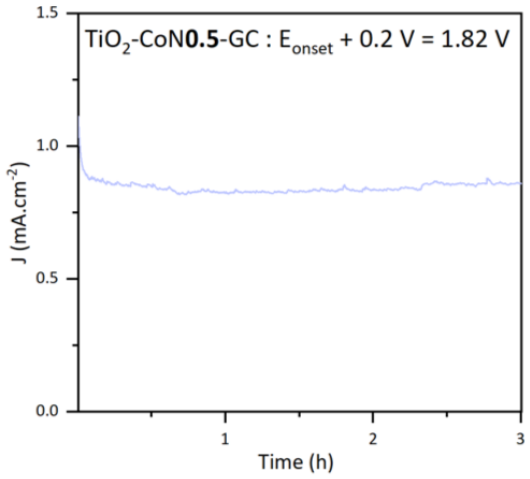

Figure 10. Photocurrent curve of the TiO_2-CoN0.5 thin film.

3. Conclusion

The synthesis of TiO_2-Co_3O_4/$Co(OH)_2$ hybrid materials by the sol-gel method has made it possible to highlight the effect of cobalt on the properties of TiO_2 thin films. First, in terms of structural and textural properties, an inversion of the dominance of the anatase and rutile phases in TiO_2 powders before and after the addition of cobalt oxide was observed: the rutile phase was dominant in the absence of cobalt, whereas it was the anatase phase in the presence of cobalt. A homogenization of crystallite and pore size and an increase in specific surface area for hybrid powders were also observed. Secondly, by optical characterization of the thin films using UV-Vis-NIR spectroscopy, it was shown that an increase in the visible absorption of the thin films is possible with the addition of cobalt oxide, and increasingly so with increasing Co/Ti ratio. Finally, the electronic properties of the thin films were characterized in two different ways: by C-AFM (at the nanoscale for volume analysis) and by EIS (at the macroscale for surface analysis). These analyses confirmed the heterogeneity of the electrical properties of the hybrid thin films due to the incorporation of the cobalt oxide. Co_3O_4 in the bulk does not improve the electrical conductivity of the materials, while $Co(OH)_2$ on the surface of the films induces a significant decrease in the charge transfer resistance. Finally, the presence of cobalt enhances the photoelectrocatalytic properties of composite thin films. The current density of cobalt-free thin films increases by a factor of 30, resulting in a maximum current of 1.570 mA.cm^{-2} at 2V for the TiO_2-CoN0.5 thin film with the highest Ti/Co ratio. The thin film's stability is demonstrated for 3 hours under xenon illumination, enabling it to theoretically produce 0.3 µmol.min^{-1}.cm^{-2} of H_2.

Given the feasibility of this synthesis method, it is possible to explore the use of other metal oxide types, such as $BiVO_4$ or Fe_2O_3, in sol-gel one-pot synthesis to investigate the advantages of such a heterojunction. Additionally, future work will focus on coupling real-time H_2 production with the photodegradation of a model pollutant in the electrolyte to qualify these materials as photoanodes for a PEC cell operating with water from real effluents.

4. Experimental Section

4.1. Synthesis procedure

The starting materials, titanium (IV) isopropoxyde (TTIP, 99.999 % trace metal basis), cobalt nitrate hexahydrate ($Co(NO_3)_2 \bullet 6\ H_2O$, ≥ 98%), and nitric acid (HNO_3, ACS reagent 70%) were all purchased from Sigma Aldrich. The three different polymeric biosurfactants are the same as those used in our previous work[35]: GBACoco (lot PF345, Surfactgreen, France – named GC), GBAC18:1 (lot PF339, Surfactgreen, France – named GB) and Lansperse BIO868 (Bio-Loop Technology, Lankem, United Kingdom – named BIO). They are all bio-based and 100 % renewable. The solutions were prepared by a sol-gel method; for TiO_2, 10 mL of TTIP was mixed with 16.85 mL of HNO_3 (2 $mol.L^{-1}$), and for TiO_2-Co_3O_4, the cobalt nitrate was further added in two different molar ratios (HNO_3/TTIP/$Co(NO_3)_2 \bullet 6\ H_2O$ = 1/1/0.25 and 1/1/0.5). Once the solution was stabilized, 1 g of surfactant was added. Then, the samples were shaped in two different forms: as powders for structural and morphological characterization and as thin films for the other characterizations. The details of the dip coating, drying and calcination steps have been reported in previous paper.[32] Samples with ratios of 1/1/0.25 and 1/1/0.5 are hereafter referred to as TiO_2-CoN0.25 and TiO_2-CoN0.5, respectively.

4.2. Materials characterizations

4.2.1. Structural characterization

Powder X-ray Diffraction (XRD) was performed using a X'pert Pro (Pan Analytical) diffractometer with Cu-Kα radiation (Kα1 1.5405980 Å, Kα2 1.5444260 Å, ratio Kα1/Kα2 1.05) operating at 40 kV and 20 mA. Diffraction patterns were collected from 20° to 60° with a step size of 0.008° and a scan rate of 0.013° per second. Rietveld refinement was performed using FullProf with CIF file of anatase phase (CollCode 92363 - Weirich T.E - 2000), rutile phase (CollCode 93097 - Ballirano P - 2001) and spinel phase (CollCode 290720 - Meena P.L - 2013). The BET (Brunauer, Emmet and Teller) specific surface area and mean pore size of the powders were measured using a Micromeritics ASAP-2010.

4.2.2. Morphological and chemical characterization

XPS analysis was performed on an ESCALAB 250 (Thermo Electron) using a monochromatic source, Al Kα, as the excitation source and photoelectron spectra were calibrated as the binding energy relative to the energy of C-C of C1s at 284.8 eV. The relative error of the XPS atomic percentages is 10%. The thickness and surface area of the thin films were observed on a Hitachi S4800 with an AztecOne energy dispersive spectrometer. The error of the estimated thickness measurement and EDX ratio is 10-20%.

4.2.3. Optical and electrical characterization

UV absorption and band gap of the thin films were investigated using an integrating sphere spectrophotometer Shimadzu UV 3600. Nanoscale conductive analysis of the thin films was performed on a Bruker Multimode 8 Atomic Force Microscope (AFM) setup equipped with a PtSi tip (radius of curvature Rc = 27 nm and spring constant k = 1.8 $N.m^{-1}$) using the conductive AFM (C-AFM) mode. A contact force of 33 nN and a current sensitivity module of
100 $nA.V^{-1}$ were applied. The current was probed over a 2 μm × 0.5 μm area at three dif-

ferent locations on each sample with good consistency. A 384 x 96 pixel matrix was used for imaging, giving a pixel size of 5.2 nm x 5.2 nm.

4.2.4. Photo-Electrochemical characterizations

Cyclic voltammetry and photocurrent experiments were monitored on a Solartron SI 1287 and impedance spectroscopy on a Solartron SI 1260. The photoelectrochemical cell was supplied by Pine Research Co USA and was equipped with a quartz window. The electrolyte was a solution of 0.01 mol.L^{-1} NaOH - 0.1 mol.L^{-1} Na_2SO_4 and the Ag/AgCl electrode was used as the reference electrode and glass carbon as the counter electrode. Cyclic voltammetry curves were measured from 0.0 V/RHE to 2.0 V/RHE at a scan rate of 50 mV.s^{-1}. The stability of the thin films was investigated by applying the onset potential + 0.2 V for 3 hours. The interfacial conductivity of the thin films was measured in the dark at the onset potential over the frequency range from 0.1 Hz to 106 Hz using an AC voltage of 10 mV amplitude.
A 75 W LOT Quantum Design xenon lamp with a wavelength range of 250-2700 nm and a power density of 3 mW.cm^{-2} was used for the illumination.

Supplementary Materials: The following supporting information can be downloaded at: www.mdpi.com/xxx/s1, Figure S1: BET results with p/p0 being the ratio of the applied N_2 pressure over the N_2 relative vapor pressure. (i) Isotherm of GC samples, (ii) Isotherm of GB samples and (iii) Isotherm of BIO samples; Figure S2: Pore size distribution for the TiO_2-CoN0.25 samples, (i) TiO_2-CoN0.25-GC, (ii)TiO_2-CoN0.25-GB and (iii) TiO_2-CoN0.25-BIO; Figure S3: Pore size distribution for the TiO_2-CoN0.5 samples, (i) TiO_2-CoN0.5-GC, (ii) TiO_2-CoN0.5-GB and (iii) TiO_2-CoN0.5-BIO; Figure S4: Nyquist plot in the dark at the onset potential for (i) TiO_2-GC (ii) TiO_2-CoN0.25-GC and (iii) TiO_2-CoN0.5-GC; Table S1: Rietveld refinement data; Table 2: Crystallite size by Scherrer formula; Table S3: Results from C-AFM characterisation; Table S4: Data from the electrochemical impedance spectroscopy.

Author Contributions: F.D. performed the experiments, analyzed the data, discussed the results, and drafted and revised the manuscript. V.F. performed XPS experiments, discussed the related results and revised the manuscript. C.V.-F. performed C-AFM experiments, discussed the related results and revised the manuscript. M.R., F.R., and S.R. discussed the results, drafted and revised the manuscript, and oversaw and validated the work. All authors have read and approved to the published version of the manuscript.

Funding: This research received no external funding.

Institutional Review Board Statement: Not applicable.

Informed Consent Statement: Not applicable.

Data Availability Statement: The data supporting the reported results can be made available upon request.

Acknowledgments: Thanks to Surfactgreen and Lankem for providing the surfactants. Thanks to Sara El Hakim and Sergueï Nikitenko of the Institut de Chimie Séparative de Marcoule (ICSM) for the use of the integrating sphere spectrophotometer. Thanks to the Ecole Nationale Supérieure de Chimie de Montpellier (ENSCM) for allowing us to use MEB and EDX.

Conflicts of Interest: The authors declare no conflict of interest.

References

1. van de Krol, R.; Grätzel, M. *Photoelectrochemical Hydrogen Production*; van de Krol, R., Grätzel, M., Eds.; Electronic Materials: Science & Technology; Springer US: Boston, MA, 2012; Vol. 102; ISBN 978-1-4614-1379-0.
2. Ahmed, M.; Dincer, I. A Review on Photoelectrochemical Hydrogen Production Systems: Challenges and Future Directions. *Int J Hydrogen Energy* **2019**, *44*, 2474–2507, doi:10.1016/j.ijhydene.2018.12.037.
3. Chiu, Y.-H.; Lai, T.-H.; Kuo, M.-Y.; Hsieh, P.-Y.; Hsu, Y.-J. Photoelectrochemical Cells for Solar Hydrogen Production: Challenges and Opportunities. *APL Mater* **2019**, *7*, doi:10.1063/1.5109785.

4. Pop, L.-C.; Tantis, I.; Lianos, P. Photoelectrocatalytic Hydrogen Production Using Nitrogen Containing Water Soluble Wastes. *Int J Hydrogen Energy* **2015**, *40*, 8304–8310, doi:10.1016/j.ijhydene.2015.04.116.
5. Wang, G.; Ling, Y.; Lu, X.; Wang, H.; Qian, F.; Tong, Y.; Li, Y. Solar Driven Hydrogen Releasing from Urea and Human Urine. *Energy Environ Sci* **2012**, *5*, 8215–8219, doi:10.1039/c2ee22087c.
6. Wang, G.; Ling, Y.; Lu, X.; Zhai, T.; Qian, F.; Tong, Y.; Li, Y. A Mechanistic Study into the Catalytic Effect of Ni(OH)2 on Hematite for Photoelectrochemical Water Oxidation. *Nanoscale* **2013**, *5*, 4129–4133, doi:10.1039/c3nr00569k.
7. Antoniadou, M.; Bouras, P.; Strataki, N.; Lianos, P. Hydrogen and Electricity Generation by Photoelectrochemical Decomposition of Ethanol over Nanocrystalline Titania. *Int J Hydrogen Energy* **2008**, *33*, 5045–5051, doi:10.1016/j.ijhydene.2008.07.005.
8. Mohapatra, S.K.; Raja, K.S.; Mahajan, V.K.; Misra, M. Efficient Photoelectrolysis of Water Using TiO2 Nanotube Arrays by Minimizing Recombination Losses with Organic Additives. *Journal of Physical Chemistry C* **2008**, *112*, 11007–11012, doi:10.1021/jp7100539.
9. Nakata, K.; Fujishima, A. TiO2 Photocatalysis: Design and Applications. *Journal of Photochemistry and Photobiology C: Photochemistry Reviews* **2012**, *13*, 169–189, doi:10.1016/j.jphotochemrev.2012.06.001.
10. Fujishima, A.; Rao, T.N.; Tryk, D.A. Titanium Dioxide Photocatalysis. *Journal of Photochemistry and Photobiology C: Photochemistry Reviews* **2000**, *1*, 1–21, doi:10.1016/S1389-5567(00)00002-2.
11. Fu, A.; HONDA, K. Electrochemical Photolysis of Water at a Semiconductor Electrode. *Nature* **1972**, *238*, 37–38, doi:10.1038/238037a0.
12. Jiang, C.; Moniz, S.J.A.; Wang, A.; Zhang, T.; Tang, J. Photoelectrochemical Devices for Solar Water Splitting-Materials and Challenges. *Chem Soc Rev* **2017**, *46*, 4645–4660, doi:10.1039/c6cs00306k.
13. Wei, X.; He, X.; Wu, P.; Gong, F.; Wang, D.; Wang, S.; Lu, S.; Zhang, J.; Xiang, S.; Kai, T.; et al. Recent Advances in the Design of Semiconductor Hollow Microspheres for Enhanced Photocatalyticv Water Splitting. *Int J Hydrogen Energy* **2021**, *46*, 27974–27996, doi:10.1016/j.ijhydene.2021.06.076.
14. Wen, J.; Li, X.; Liu, W.; Fang, Y.; Xie, J.; Xu, Y. Photocatalysis Fundamentals and Surface Modification of TiO2 Nanomaterials. *Cuihua Xuebao/Chinese Journal of Catalysis* **2015**, *36*, 2049–2070, doi:10.1016/S1872-2067(15)60999-8.
15. Zheng, L.; Teng, F.; Ye, X.; Zheng, H.; Fang, X. Photo/Electrochemical Applications of Metal Sulfide/TiO 2 Heterostructures. *Adv Energy Mater* **2020**, *10*, 1902355, doi:10.1002/aenm.201902355.
16. Guaraldo, T.T.; Gonçales, V.R.; Silva, B.F.; de Torresi, S.I.C.; Zanoni, M.V.B. Hydrogen Production and Simultaneous Photoelectrocatalytic Pollutant Oxidation Using a TiO2/WO3 Nanostructured Photoanode under Visible Light Irradiation. *Journal of Electroanalytical Chemistry* **2016**, *765*, 188–196, doi:10.1016/j.jelechem.2015.07.034.
17. Guo, L.; Yang, Z.; Marcus, K.; Li, Z.; Luo, B.; Zhou, L.; Wang, X.; Du, Y.; Yang, Y. MoS 2 /TiO 2 Heterostructures as Nonmetal Plasmonic Photocatalysts for Highly Efficient Hydrogen Evolution. *Energy Environ Sci* **2018**, *11*, 106–114, doi:10.1039/C7EE02464A.
18. Kumar, S.G.; Rao, K.S.R.K. Comparison of Modification Strategies towards Enhanced Charge Carrier Separation and Photocatalytic Degradation Activity of Metal Oxide Semiconductors (TiO 2 , WO 3 and ZnO). *Appl Surf Sci* **2017**, *391*, 124–148, doi:10.1016/j.apsusc.2016.07.081.
19. Mei, J.; Liao, T.; Ayoko, G.A.; Bell, J.; Sun, Z. Cobalt Oxide-Based Nanoarchitectures for Electrochemical Energy Applications. *Prog Mater Sci* **2019**, *103*, 596–677, doi:10.1016/j.pmatsci.2019.03.001.

20. Ma, J.; Wei, H.; Liu, Y.; Ren, X.; Li, Y.; Wang, F.; Han, X.; Xu, E.; Cao, X.; Wang, G.; et al. Application of Co3O4-Based Materials in Electrocatalytic Hydrogen Evolution Reaction: A Review. *Int J Hydrogen Energy* **2020**, *45*, 21205–21220, doi:10.1016/j.ijhydene.2020.05.280.
21. Cheng, C.S.; Serizawa, M.; Sakata, H.; Hirayama, T. Electrical Conductivity of Co3O4 Films Prepared by Chemical Vapour Deposition. *Mater Chem Phys* **1998**, *53*, 225–230, doi:10.1016/S0254-0584(98)00044-3.
22. Ebadi, M.; Mat-Teridi, M.A.; Sulaiman, M.Y.; Basirun, W.J.; Asim, N.; Ludin, N.A.; Ibrahim, M.A.; Sopian, K. Electrodeposited P-Type Co 3 O 4 with High Photoelectrochemical Performance in Aqueous Medium. *RSC Adv* **2015**, *5*, 36820–36827, doi:10.1039/C5RA04008F.
23. Thota, S.; Kumar, A.; Kumar, J. Optical, Electrical and Magnetic Properties of Co3O4 Nanocrystallites Obtained by Thermal Decomposition of Sol–Gel Derived Oxalates. *Materials Science and Engineering: B* **2009**, *164*, 30–37, doi:10.1016/j.mseb.2009.06.002.
24. Patel, M.; Kim, J. Thickness-Dependent Photoelectrochemical Properties of a Semitransparent Co 3 O 4 Photocathode. *Beilstein Journal of Nanotechnology* **2018**, *9*, 2432–2442, doi:10.3762/bjnano.9.228.
25. Qiao, L.; Xiao, H.Y.; Meyer, H.M.; Sun, J.N.; Rouleau, C.M.; Puretzky, A.A.; Geohegan, D.B.; Ivanov, I.N.; Yoon, M.; Weber, W.J.; et al. Nature of the Band Gap and Origin of the Electro-/Photo-Activity of Co3O4. *J Mater Chem C Mater* **2013**, *1*, 4628, doi:10.1039/c3tc30861h.
26. Liu, J.; Ke, J.; Li, Y.; Liu, B.; Wang, L.; Xiao, H.; Wang, S. Co3O4 Quantum Dots/TiO2 Nanobelt Hybrids for Highly Efficient Photocatalytic Overall Water Splitting. *Appl Catal B* **2018**, *236*, 396–403, doi:10.1016/j.apcatb.2018.05.042.
27. Wang, Y.; Zhu, C.; Zuo, G.; Guo, Y.; Xiao, W.; Dai, Y.; Kong, J.; Xu, X.; Zhou, Y.; Xie, A.; et al. 0D/2D Co3O4/TiO2 Z-Scheme Heterojunction for Boosted Photocatalytic Degradation and Mechanism Investigation. *Appl Catal B* **2020**, *278*, 119298, doi:10.1016/j.apcatb.2020.119298.
28. Dai, G.; Liu, S.; Liang, Y.; Luo, T. Synthesis and Enhanced Photoelectrocatalytic Activity of p–n Junction Co3O4/TiO2 Nanotube Arrays. *Appl Surf Sci* **2013**, *264*, 157–161, doi:10.1016/j.apsusc.2012.09.160.
29. Zhao, X.-R.; Cao, Y.-Q.; Chen, J.; Zhu, L.; Qian, X.; Li, A.-D.; Wu, D. Photocatalytic Properties of Co3O4-Coated TiO2 Powders Prepared by Plasma-Enhanced Atomic Layer Deposition. *Nanoscale Res Lett* **2017**, *12*, 497, doi:10.1186/s11671-017-2269-4.
30. Miquelot, A. Propriétés Structurales, Optiques et Électriques d'hétérojonctions Co3O4/TiO2 Déposées Par MOCVD Pour l'étude de La Production de H2 Par Dissociation Photocatalytique de l'eau, Université de Toulouse, 2019.
31. Saeed, M.; Usman, M.; Ibrahim, M.; Haq, A. ul; Khan, I.; Ijaz, H.; Akram, F. Enhanced Photo Catalytic Degradation of Methyl Orange Using p–n Co 3 O 4 -TiO 2 Hetero-Junction as Catalyst. *International Journal of Chemical Reactor Engineering* **2020**, *18*, doi:10.1515/ijcre-2020-0004.
32. Thamaphat, K.; Limsuwan, P.; Ngotawornchai, B. Phase Characterization of TiO 2 Powder by XRD and TEM. *Kasetsart J. (Nat. Sci.)* **2008**, *42*, 357–361.
33. Itteboina, R.; Sau, T.K. Sol-Gel Synthesis and Characterizations of Morphology-Controlled Co3O4 Particles. *Mater Today Proc* **2019**, *9*, 458–467, doi:10.1016/j.matpr.2019.02.176.
34. Rietveld, H.M. A Profile Refinement Method for Nuclear and Magnetic Structures. *J Appl Crystallogr* **1969**, *2*, 65–71, doi:10.1107/s0021889869006558.
35. Duquet, F.; Nada, A.A.; Rivallin, M.; Rouessac, F.; Villeneuve-Faure, C.; Roualdes, S. Influence of Bio-Based Surfactants on TiO2 Thin Films as Photoanodes for Electro-Photocatalysis. *Catalysts* **2021**, *11*, 1228, doi:10.3390/catal11101228.

36. Gotić, M.; Ivanda, M.; Sekulić, A.; Musić, S.; Popović, S.; Turković, A.; Furić, K. Microstructure of Nanosized TiO2 Obtained by Sol-Gel Synthesis. *Mater Lett* **1996**, *28*, 225–229, doi:10.1016/0167-577X(96)00061-4.
37. Arconada, N.; Durán, A.; Suárez, S.; Portela, R.; Coronado, J.M.; Sánchez, B.; Castro, Y. Synthesis and Photocatalytic Properties of Dense and Porous TiO2-Anatase Thin Films Prepared by Sol–Gel. *Appl Catal B* **2009**, *86*, 1–7, doi:10.1016/j.apcatb.2008.07.021.
38. Šegota, S.; Ćurković, L.; Ljubas, D.; Svetličić, V.; Houra, I.F.; Tomašić, N. Synthesis, Characterization and Photocatalytic Properties of Sol–Gel TiO2 Films. *Ceram Int* **2011**, *37*, 1153–1160, doi:10.1016/j.ceramint.2010.10.034.
39. Brisk, M.A.; Baker, A.D. Shake-up Satellites in X-Ray Photoelectron Spectroscopy. *J Electron Spectros Relat Phenomena* **1975**, *7*, 197–213, doi:10.1016/0368-2048(75)80061-2.
40. Svensson, S.; Eriksson, B.; Mårtensson, N.; Wendin, G.; Gelius, U. Electron Shake-up and Correlation Satellites and Continuum Shake-off Distributions in X-Ray Photoelectron Spectra of the Rare Gas Atoms. *J Electron Spectros Relat Phenomena* **1988**, *47*, 327–384, doi:10.1016/0368-2048(88)85020-5.
41. Biesinger, M.C.; Payne, B.P.; Grosvenor, A.P.; Lau, L.W.M.; Gerson, A.R.; Smart, R.S.C. Resolving Surface Chemical States in XPS Analysis of First Row Transition Metals, Oxides and Hydroxides: Cr, Mn, Fe, Co and Ni. *Appl Surf Sci* **2011**, *257*, 2717–2730, doi:10.1016/j.apsusc.2010.10.051.
42. Xu, F.; Zhang, L.; Cheng, B.; Yu, J. Direct Z-Scheme TiO 2 /NiS Core–Shell Hybrid Nanofibers with Enhanced Photocatalytic H 2 -Production Activity. *ACS Sustain Chem Eng* **2018**, *6*, 12291–12298, doi:10.1021/acssuschemeng.8b02710.
43. Zhu, H.; Zhang, J.; Yanzhang, R.; Du, M.; Wang, Q.; Gao, G.; Wu, J.; Wu, G.; Zhang, M.; Liu, B.; et al. When Cubic Cobalt Sulfide Meets Layered Molybdenum Disulfide: A Core–Shell System Toward Synergetic Electrocatalytic Water Splitting. *Advanced Materials* **2015**, *27*, 4752–4759, doi:10.1002/adma.201501969.
44. Bredar, A.R.C.; Chown, A.L.; Burton, A.R.; Farnum, B.H. Electrochemical Impedance Spectroscopy of Metal Oxide Electrodes for Energy Applications. *ACS Appl Energy Mater* **2020**, *3*, 66–98, doi:10.1021/acsaem.9b01965.